Non-Copper Metal Catalyzing Deep CO_2 Electroreduction to Hydrocarbon

Chaojie Chen, Xiaowan Bai, Yan Jiao, Yao Zheng*, and Shi-Zhang Qiao*

School of Chemical Engineering, The University of Adelaide, Adelaide, SA 5005, Australia

E-mail: yao.zheng01@adelaide.edu.au, s.qiao@adelaide.edu.au

Supplementary Methods

Preparation of Pd/Ga/Zn/Ag/Au catalysts. In a typical experiment, 600 mg Potassium Bromide (KBr), 105 mg polyvinylpyrrolidone (PVP), and 60 mg sodium ascorbate were dissolved into 8 mL H_2O to form a transparent solution and the solution was heated at 80 ℃ for 30 minutes. Then, 58 mg sodium tetrachloropalladate (Na_2PdCl_4)/60 mg zinc nitrate ($Zn(NO_3)_2$)/80 mg gallium nitrate ($Ga(NO_3)_3$) was added into the solution and heated for 3 h. Finally, Pd/Zn/Ga catalysts was obtained by centrifugation for 20 minutes and dried at 60 ℃ for 1 h.

The Ag/C and Au/C were purchased from fuel cell store.

Electrochemical CO_2 reduction reaction in the flow cell. The Nafion and anion exchange membrane (AEM, FAB-PK-130) were purchased from Fuel Cell Store (USA). The CO_2RR performance of obtained catalysts were investigated in a commercial flow cell (Gassunion). 5 mg catalysts were dispersed into 960 μL ethanol and 40 μL Nafion solution (5 wt%) to prepare catalyst ink. The working electrodes were fabricated by spraying ink onto gas diffusion electrodes (YLS 30T) at 70 ℃. The electrode area is 2*0.5 cm^2 and the mass loadings are controlled at 0.6-0.8 mg cm^{-2}. The Ag/AgCl electrode and Pt foil were respectively employed as reference electrode and counter electrode. The gas flow for CO_2 is 40 sccm and the liquid flow rate of 1 M KOH is 10 mL min^{-1}. The CO_2RR performance were conducted through chronopotentiometry on a CHI 760E electrochemical station. The catalysts were pre-activated at various currents for 300s in the flow cell before investigating CO_2RR performance. The Gas Chromatography (GC, Agilent 8890) was employed to analyze gas products.

The Faradic efficiency is calculated according to the equation:

$$FE = (n*F*e)/Q = (n*F*e)/(I*t) \quad (1)$$

In which n corresponds to amounts of products (in moles), F is the Faradic constant, e means transferred electrons number, I is the current, and t means running time.

Recorded potentials were referenced to RHE scale through the equation:

$$E_{RHE} = E_{vs\ Ag/AgCl} + 0.197 + 0.0591 * pH \quad (2)$$

CO stripping test. For the CO stripping test, the electrolyte was 1 M $KHCO_3$ solution bubbled with CO with a potential held at –0.6 V vs. Ag/AgCl for 5 min. Immediately after this, the sparging gas was changed from CO to Ar for another 10 min to remove excess CO gas in the solution. Then the CO stripping cyclic voltammetry curves were collected at 20 mV s^{-1} in the potential ranging from –0.6 V to 0.8 V vs. Ag/AgCl. For CO stripping curves of Pd catalysts with pre-activation, catalysts were first pre-activated at corresponding voltages.

***In-situ* Attenuated Total Reflectance Infrared (ATR-IR) spectroscopy.** *In-situ* ATR-IR was conducted on a Thermo-Fisher Nicolet iS20 equipped with a liquid nitrogen-cooled HgCdTe (MCT)

detector using a VeeMax III ATR accessory (Pike Technologies). A germanium prism (60°, PIKE Technologies) was embedded in a PIKE electrochemical three-electrode cell as the working electrode with an Ag/AgCl reference electrode (Pine Research) and a platinum-wire counter electrode. 1 M $KHCO_3$ with CO_2-saturated was employed as electrolyte. The Pd catalysts were pre-activated at corresponding potential for 10 min before collecting curves. The measurements were all obtained by 64 scans at a spectral resolution of 4 cm^{-1}.

***In-situ* Raman spectra.** *Operando* Raman spectroscopy was performed using a confocal Raman microscope (Horiba LabRAM HR Evolution) with a 60X (1.0 N. A) water-immersion objective (Olympus). The wavelength was 532 nm. A commercial flow cell (Gaossunion) was employed as reactor for *in-situ* Raman spectra. The Pd catalyst on the GDE acted as the working electrode, an Ag/AgCl electrode was reference electrode, and the carbon electrode was employed as counter electrode. 1 M KOH was electrolyte and the gas flow rate for the Raman test was 20 sccm. Before collecting the Raman spectra, the Pd catalyst in the cell was pre-activated at various potentials.

Materials characterization. The Scanning Electron Microscopy (SEM) was conducted on a FEI Quanta 450. The Transmission Electron Microscopy (TEM) images were characterized by a FEI Tecnai G2 Spirit TEM. The X-ray powder diffraction (XRD) data were obtained on a Rigaku MiniFlex 600 X-Ray Diffractometer using Cu Kα radiation (λ = 1.5406 Å, scan rate = 2.35° min^{-1}).

DFT calculation methods. All calculations were carried out using spin-polarized density functional theory (DFT) as implemented in the Vienna ab initio simulation package (VASP).[1] The Perdew–Burke–Ernzerhof (PBE) functional of the generalized gradient approximation (GGA) was used for electron exchange-correlation.[2] The projector augmented-wave (PAW) method was adopted to describe the core−valence interaction and a plane-wave cutoff energy was set to 400 eV.[3] During the geometry optimization, a force of 0.03 eV/Å and an energy of 10^{-5} eV on each relaxed atom were chosen as the convergence threshold. The density functional dispersion correction was considered by using the DFT-D3 method to describe the van der Waals interactions.[4] The Pd(111) surface was modeled by a four-layered slab of 4 × 4 supercell with a vacuum space of 15 Å, where the bottom two layers were fixed during the structure optimization calculation, using a (3 × 3 × 1) Gamma centered Monkhorst-Pack k-point grid sampling. The Cu(111) surface was chosen to compare the adsorption energy of *CO without *OH adsorption.

As the number (n=0, 1, 2, 3, 4, 5, and 6) of *OH adsorbed increases, the adsorption energies of *CO are calculated on the Pd(111) surface by

$$\Delta E(*CO) = E(*CO\text{-}n*OH) - E(n*OH) - E(CO) \quad (3)$$

in which E(*CO-n*OH), E(n*OH) and E(CO) are the total energy of *CO and n*OH adsorbed on Pd(111), the energy of n*OH adsorbed on Pd(111) and the energy of CO molecules, respectively.

To assess the difficulty of *CO hydrogenation to *CHO or *COH, the Gibbs free energy barriers were calculated under different numbers of *OH adsorption by computational hydrogen electrode (CHE) model.[5] The Gibbs free energy change (ΔG) for *CO + H^+ + e^- → *CHO/*COH can be calculated by

$$\Delta G = \Delta E + \Delta E_{ZPE} - T\Delta S \quad (4)$$

where ΔE is the energy difference between the *CO, 1/2 H_2 and *CHO/*COH from DFT computations; ΔE_{ZPE} and ΔS are the changes in zero-point energies and entropies, respectively, which are obtained from the vibrational frequency calculations; T is the temperature at 298 K. The energy corrections of gas-phase species, *CO, *CHO and *COH in this work, including zero point energies and entropies, are listed in **Table S3**.

Supplementary Results

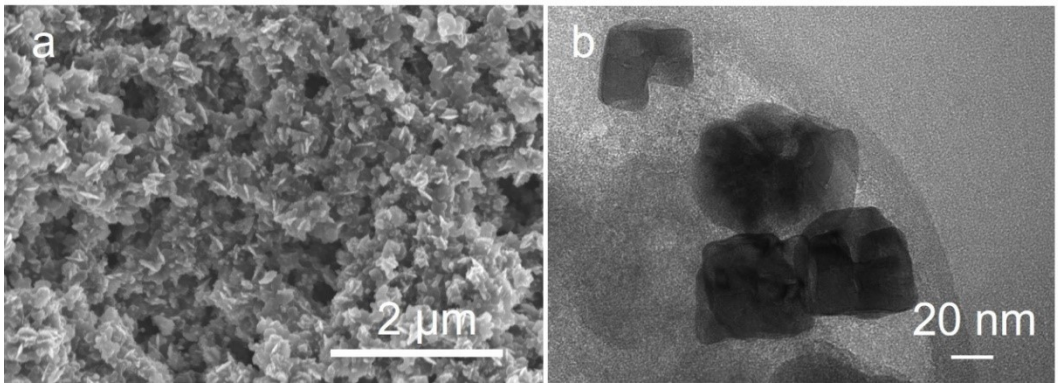

Figure S1. (a) SEM image and (b) TEM image of synthesized Pd catalysts.

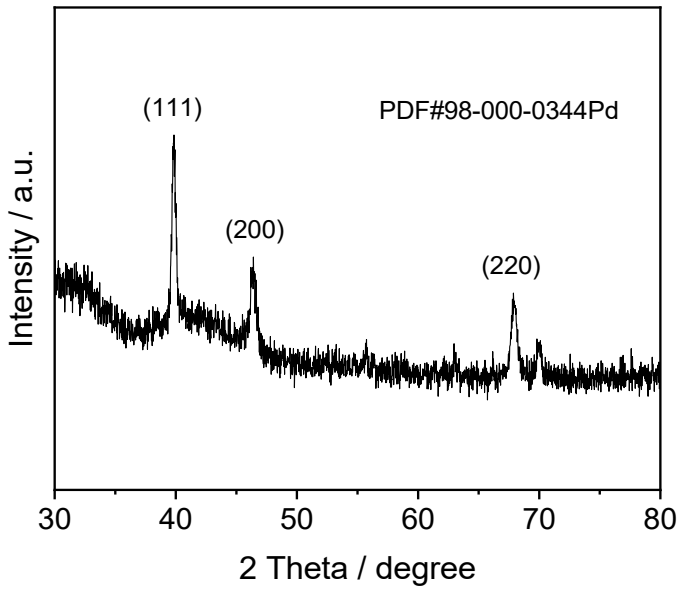

Figure S2. XRD pattern of prepared Pd catalyst.

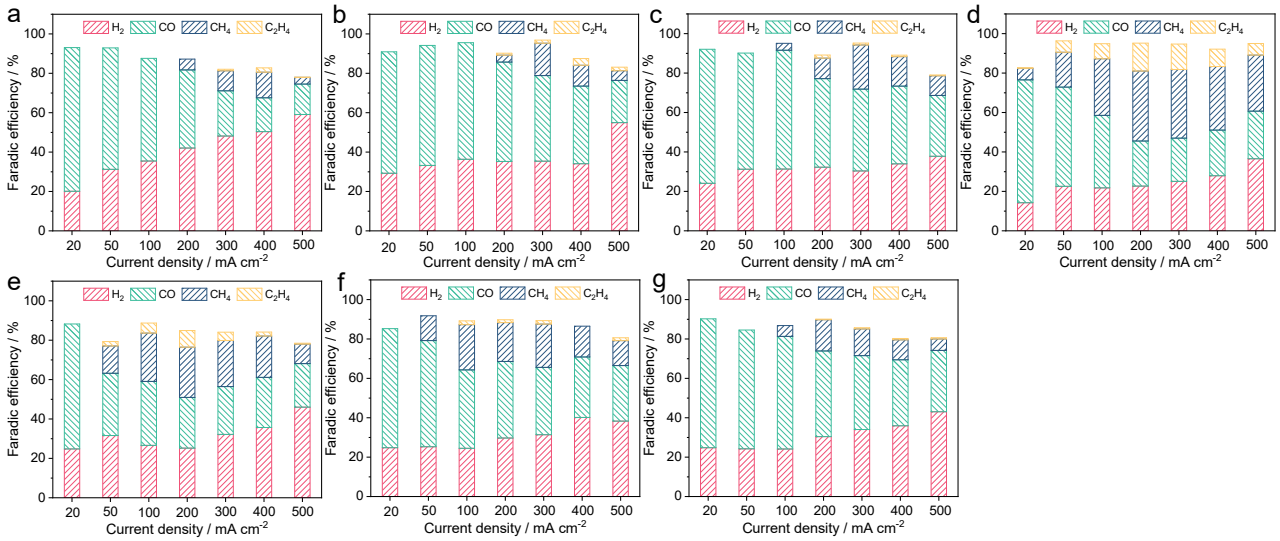

Figure S3. The CO_2RR performance of Pd catalysts (a) at fresh state, activated at (b) 50 mA cm^{-2}, (c) 100 mA cm^{-2}, (d) 200 mA cm^{-2}, (e) 300 mA cm^{-2}, (f) 400 mA cm^{-2}, and (g) 500 mA cm^{-2}

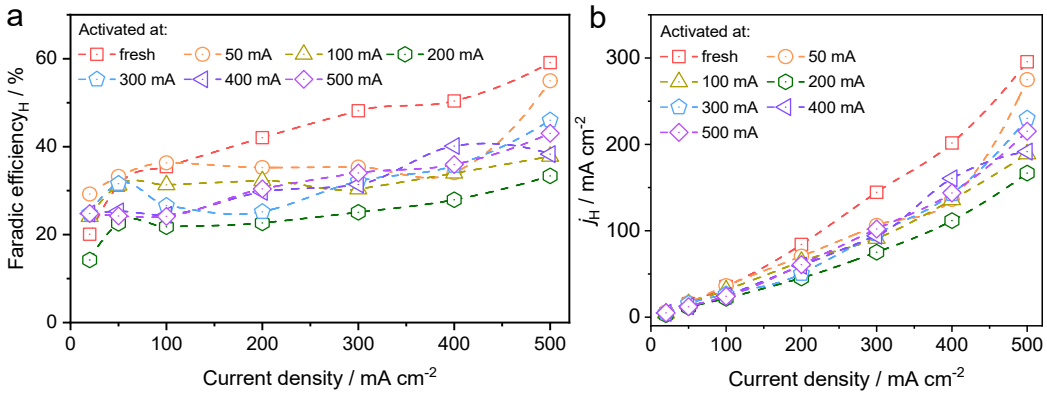

Figure S4. (a) The FE and (b) partial current densities to H_2 on Pd catalysts at diverse states.

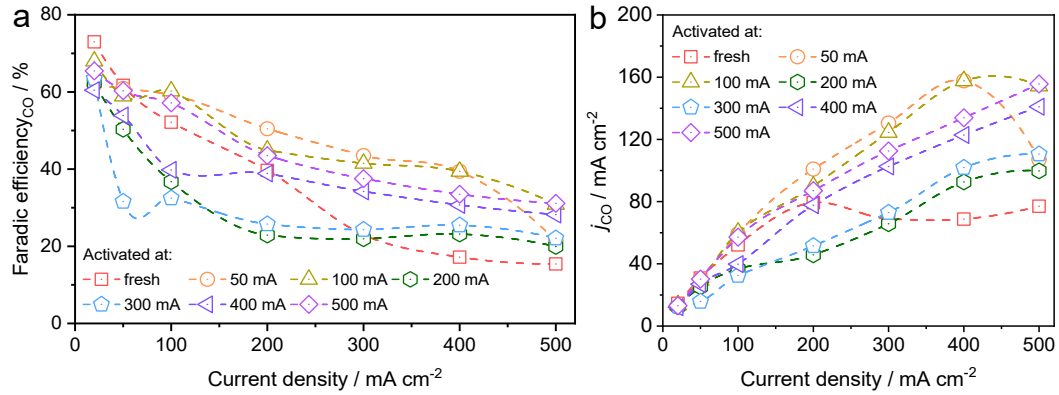

Figure S5. (a) The FE and (b) partial current densities to CO on Pd catalysts at diverse states.

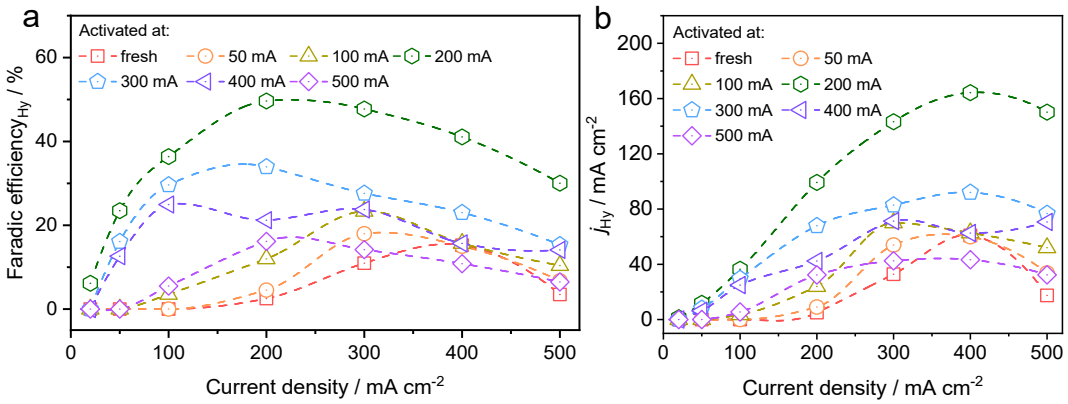

Figure S6. (a) The FE and (b) partial current densities to hydrocarbon (CH_4 + C_2H_4) on Pd catalysts at diverse states.

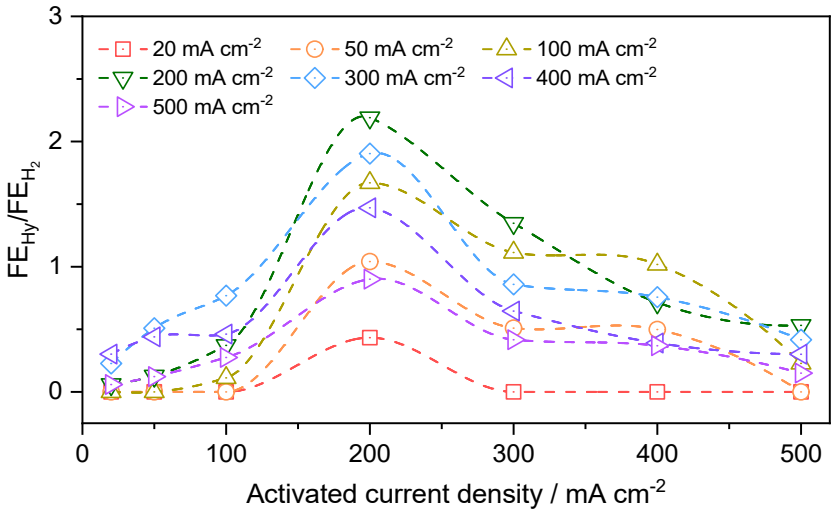

Figure S7. The FE_{Hy}/FE_{H_2} ratios on Pd catalysts at various states. The FE_{Hy}/FE_{H_2} is calculated as the ratio of FE_{Hy} to FE_{H_2}.

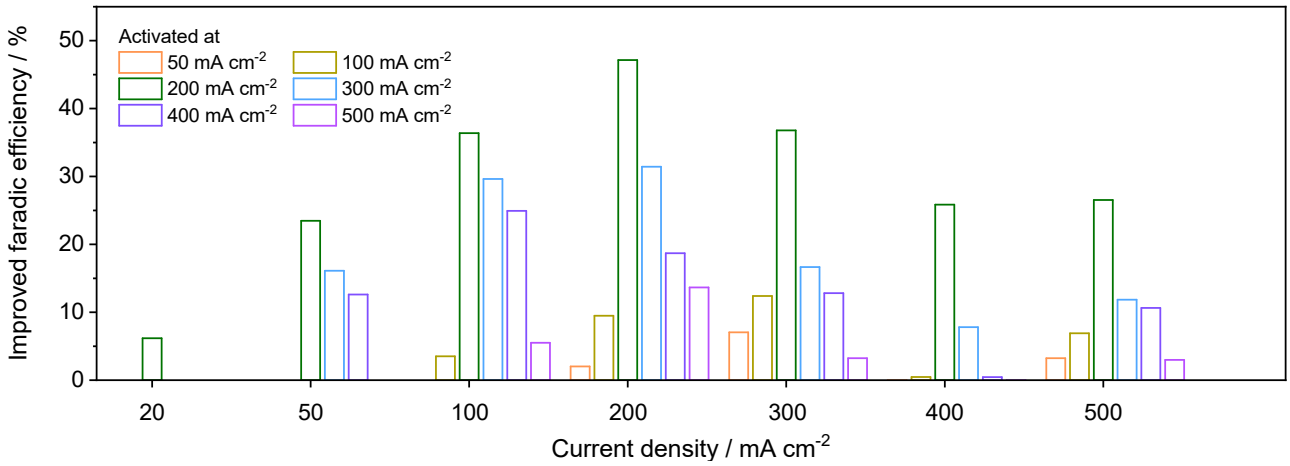

Figure S8. The improved FE to hydrocarbon on Pd activated at various current densities compared to fresh Pd catalyst.

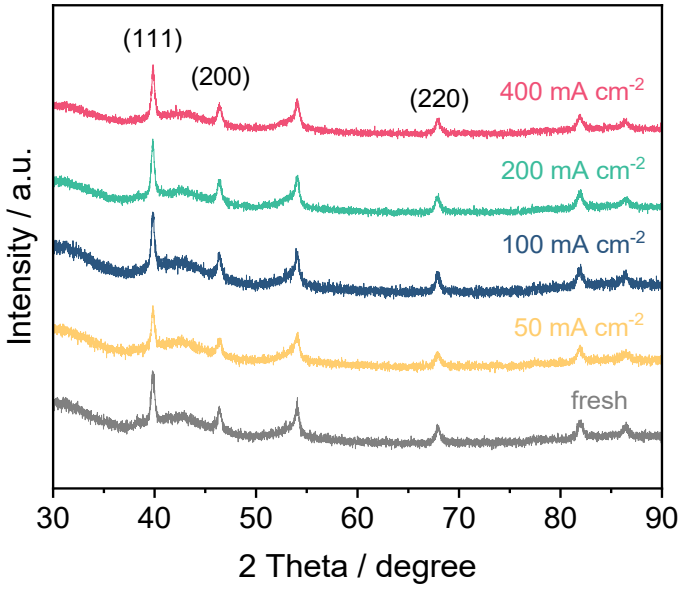

Figure S9. The XRD patterns of Pd catalysts at various states.

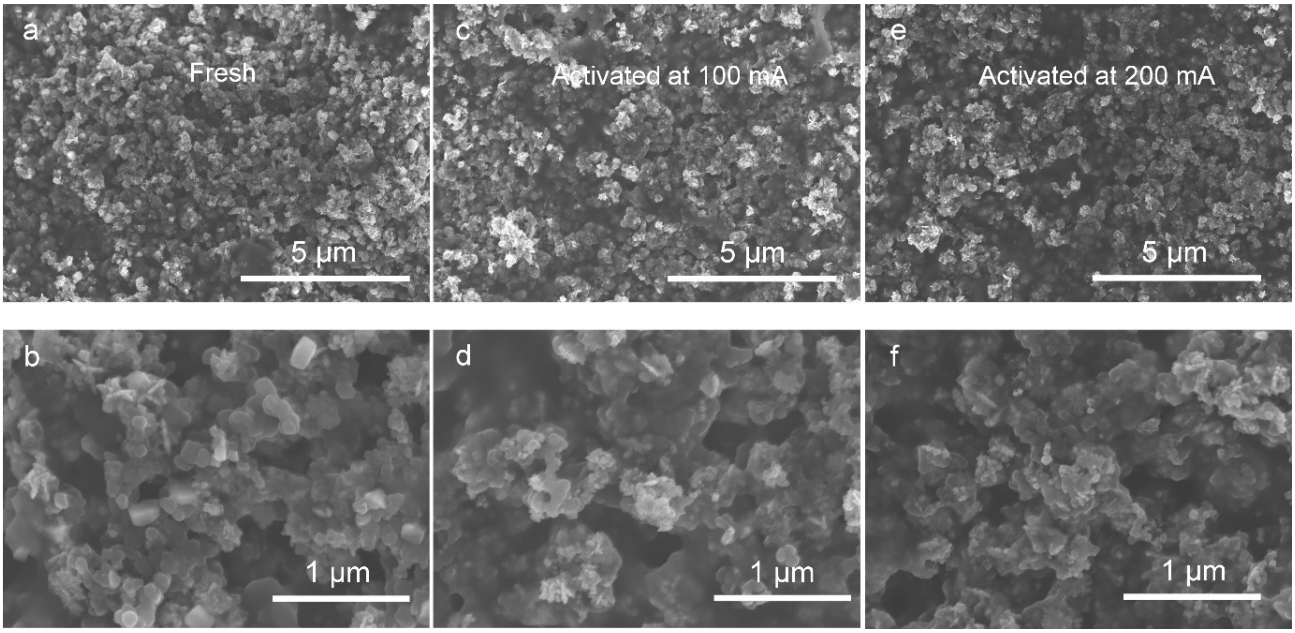

Figure S10. The SEM images of (a, b) fresh Pd catalysts and Pd catalysts activated at (c, d) 100 mA cm^{-2} and (e, f) 200 mA cm^{-2}.

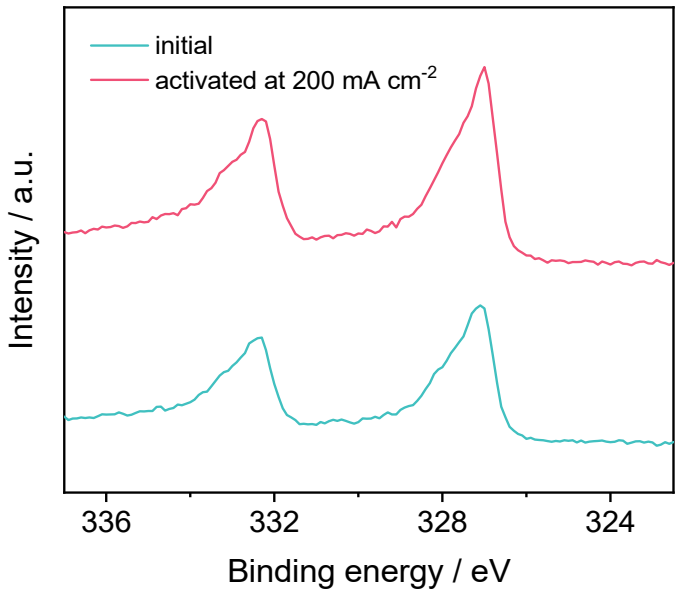

Figure S11. The XPS spectra of Pd 3d on the Pd catalysts at initial and activated at 200 mA cm^{-2}.

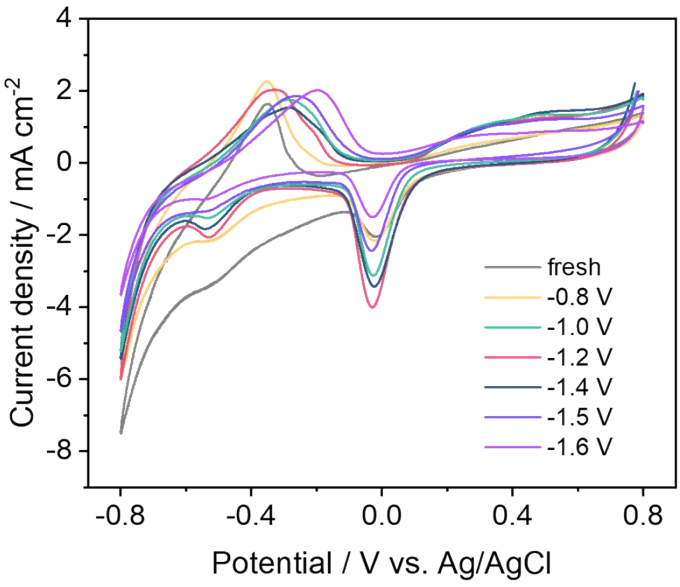

Figure S12. The CV curves of Pd catalysts at various states.

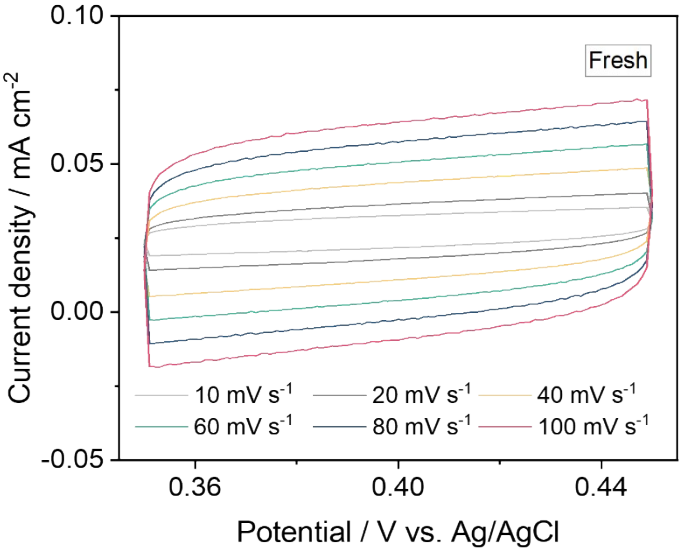

Figure S13. CV curves of fresh Pd catalyst with different scan rates of 10-100 mV s^{-1}.

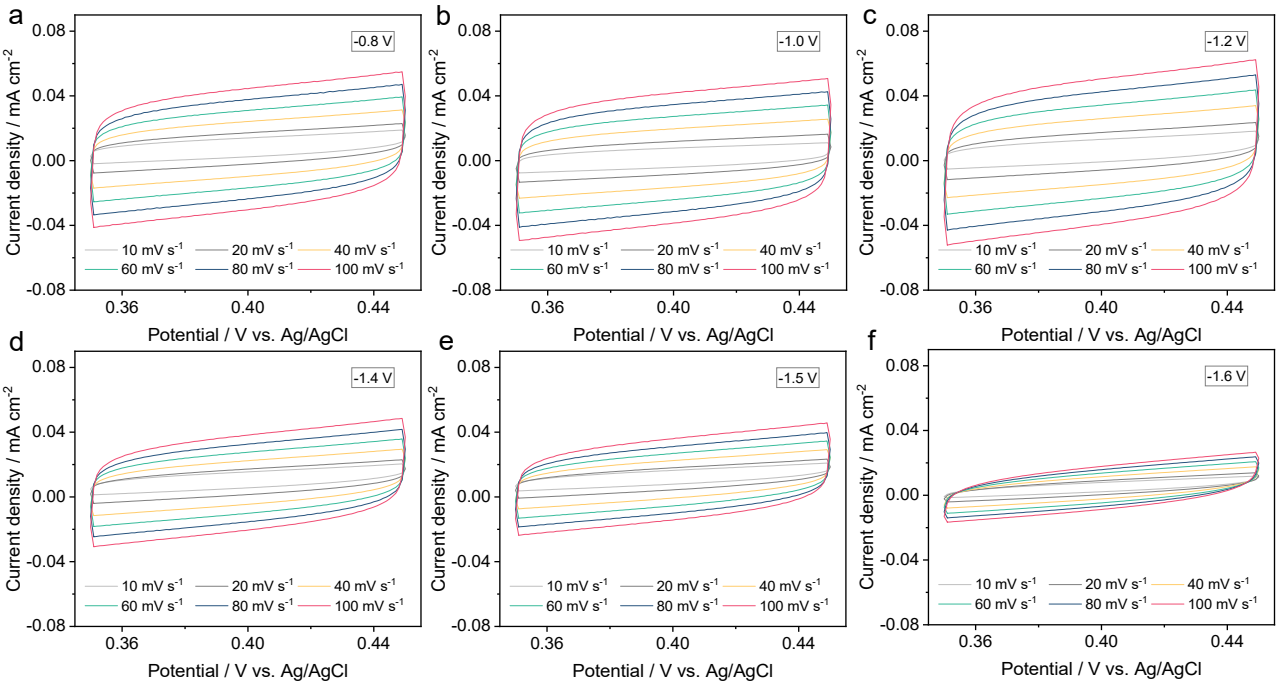

Figure S14. CV curves of fresh Pd catalysts activated at (a) –0.8 V, (b) –1.0 V, (c) –1.2 V, (d) –1.4 V, (e) –1.5 V, and (f) –1.6 V with different scan rates of 10-100 mV s^{-1}.

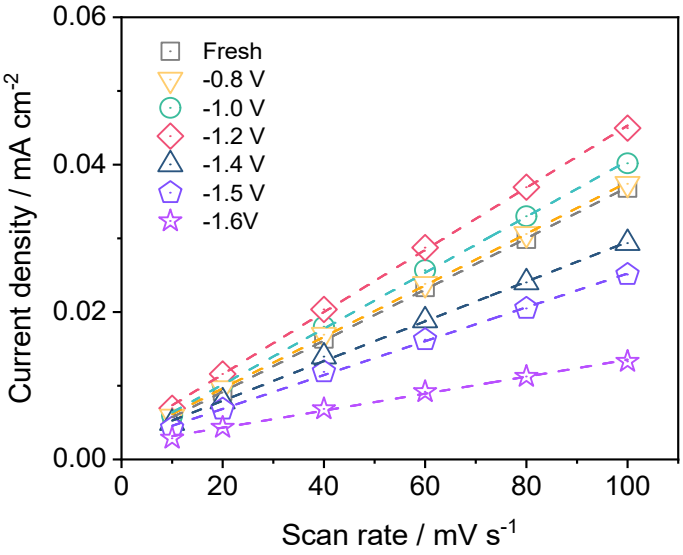

Figure S15. Double layer capacitance (C_{dl}) of Pd catalysts at various states.

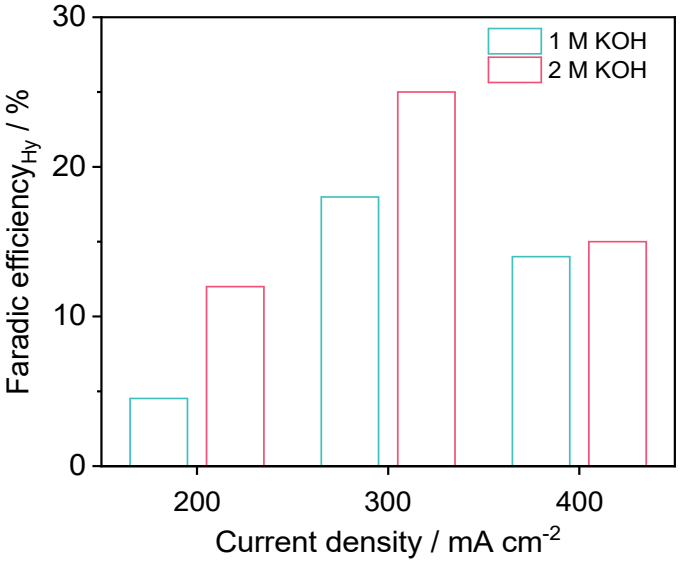

Figure S16. The CO_2RR performance of Pd catalysts activated at 50 mA cm^{-2} in 2 M KOH solution.

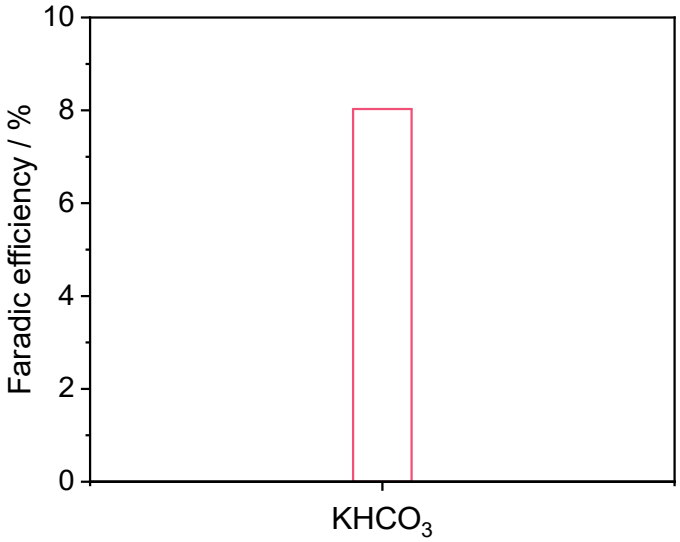

Figure S17. The FE_{Hy} at 100 mA cm^{-2} on Pd activated at 200 mA cm^{-2} in 1 M $KHCO_3$ electrolytes.

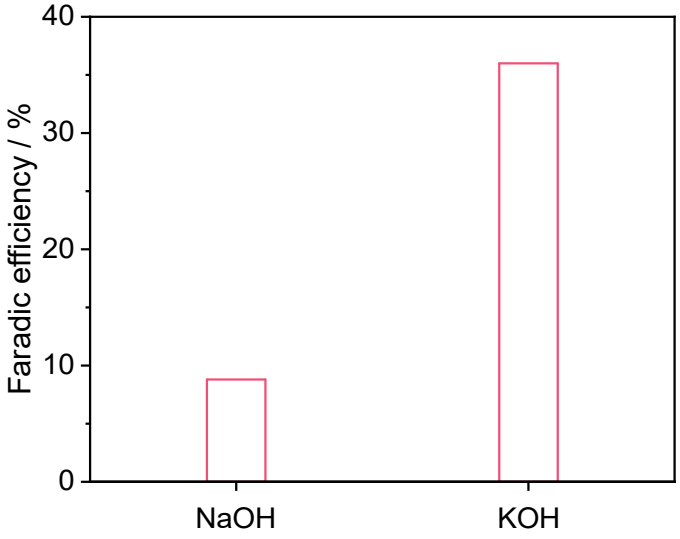

Figure S18. The comparison of FE_{Hy} at 100 mA cm^{-2} on Pd activated at 200 mA cm^{-2} in 1 M NaOH and KOH electrolytes.

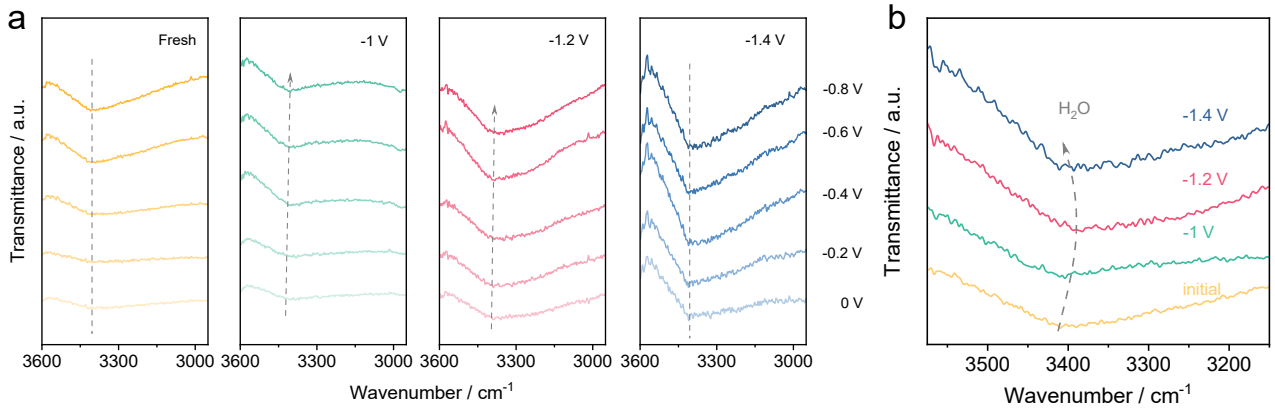

Figure S19. (a) The *in-situ* ATR-IR spectra of Pd catalysts at various states, and (b) comparison of curves collected at –0.8 V vs. RHE.

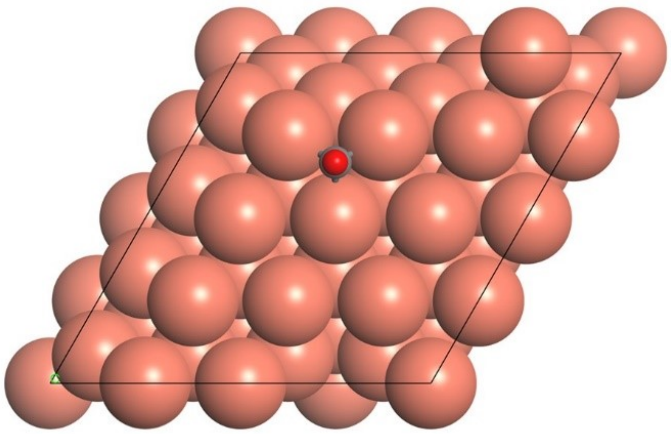

ΔE(*CO) = -0.73 eV

Figure S20. *CO adsorption on the Cu(111) surface.

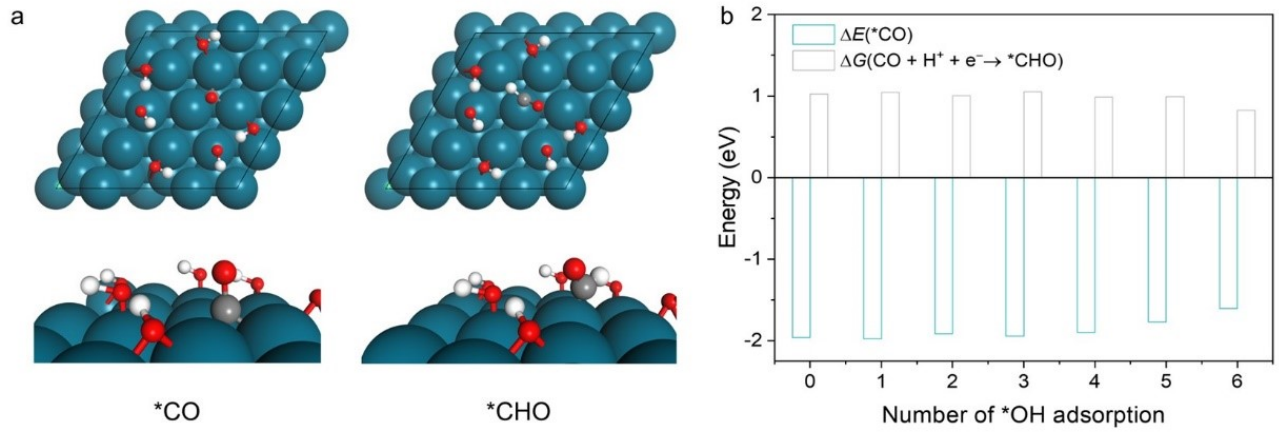

Figure S21. (a) The top and side views of *CO and *CHO with 6 *OH adsorbed on the Pd(111) surface. (b) Changes in the adsorption energy of *CO and the free energy barrier for the hydrogenation of *CO to *CHO as the number of *OH adsorption increases.

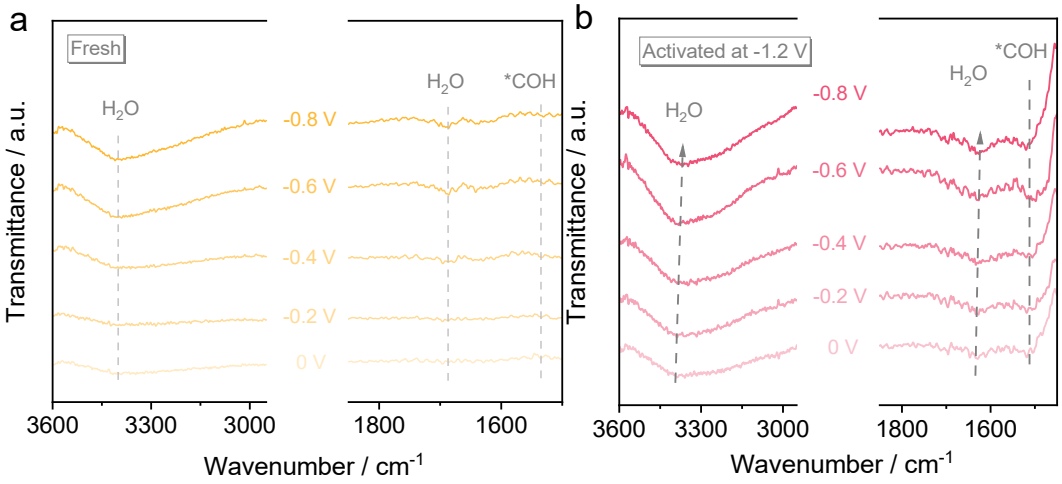

Figure S22. The *in-situ* ATR-IR spectra of (a) fresh Pd catalyst and (b) Pd catalyst activated at –1.2 V.

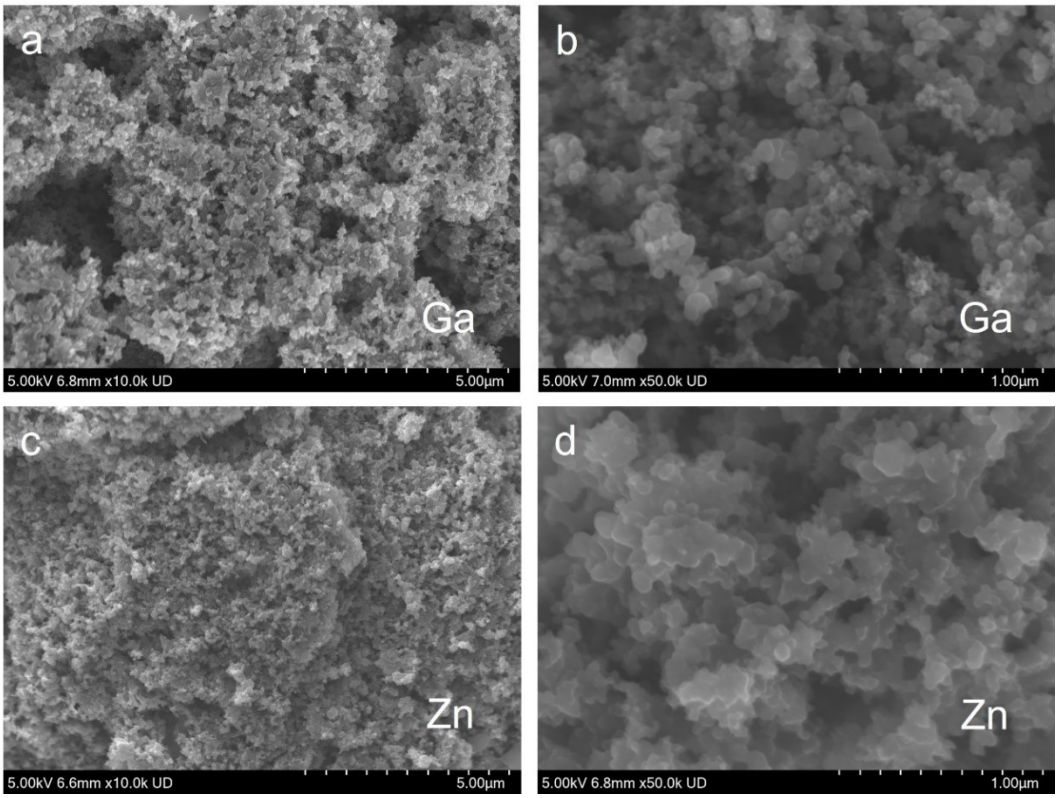

Figure S23. The SEM images of (a, b) Ga catalysts and (c, d) Zn catalysts.

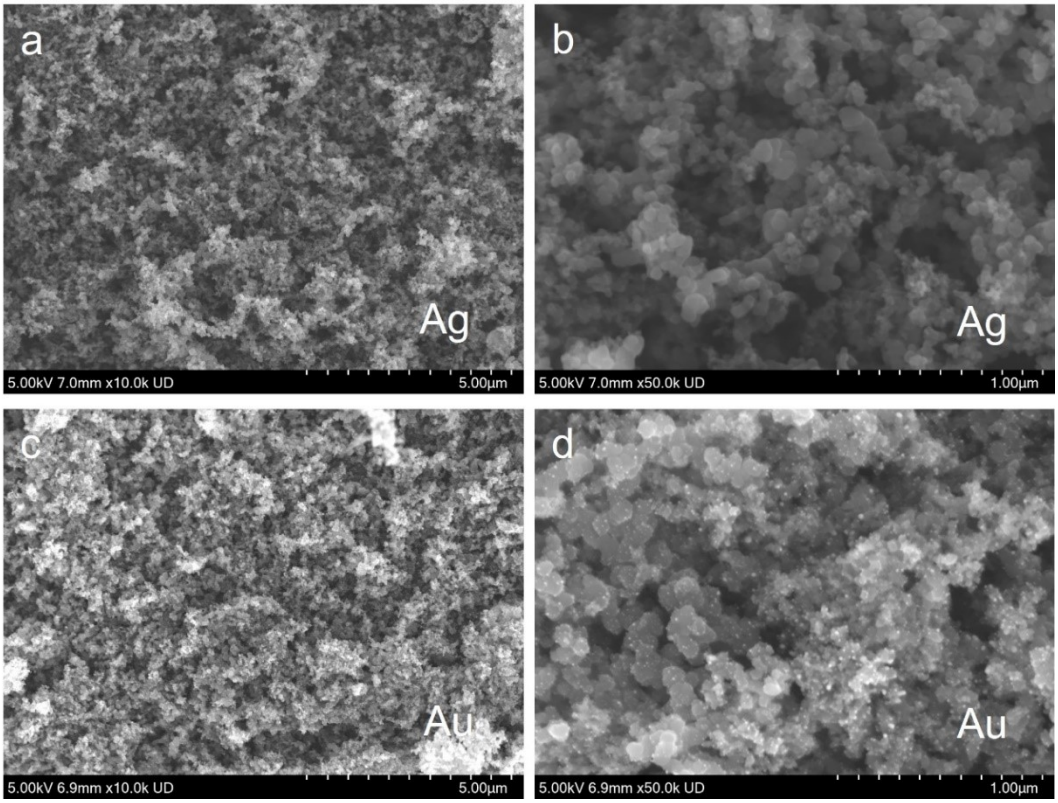

Figure S24. The SEM images of commercial (a, b) Ag catalysts and (c, d) Au catalysts.

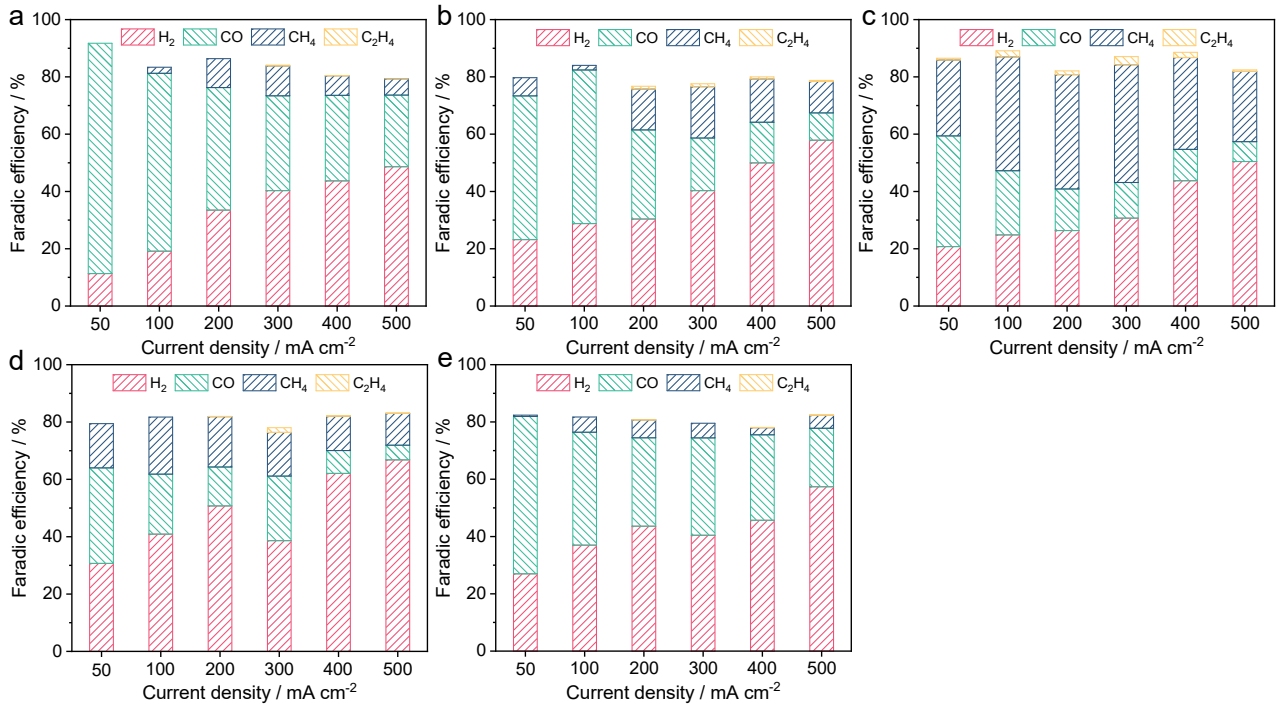

Figure S25. The CO_2RR performance of Ag catalysts (a) at fresh state, activated at (b) 100 mA cm^{-2}, (c) 200 mA cm^{-2}, (d) 300 mA cm^{-2} and (e) 400 mA cm^{-2}.

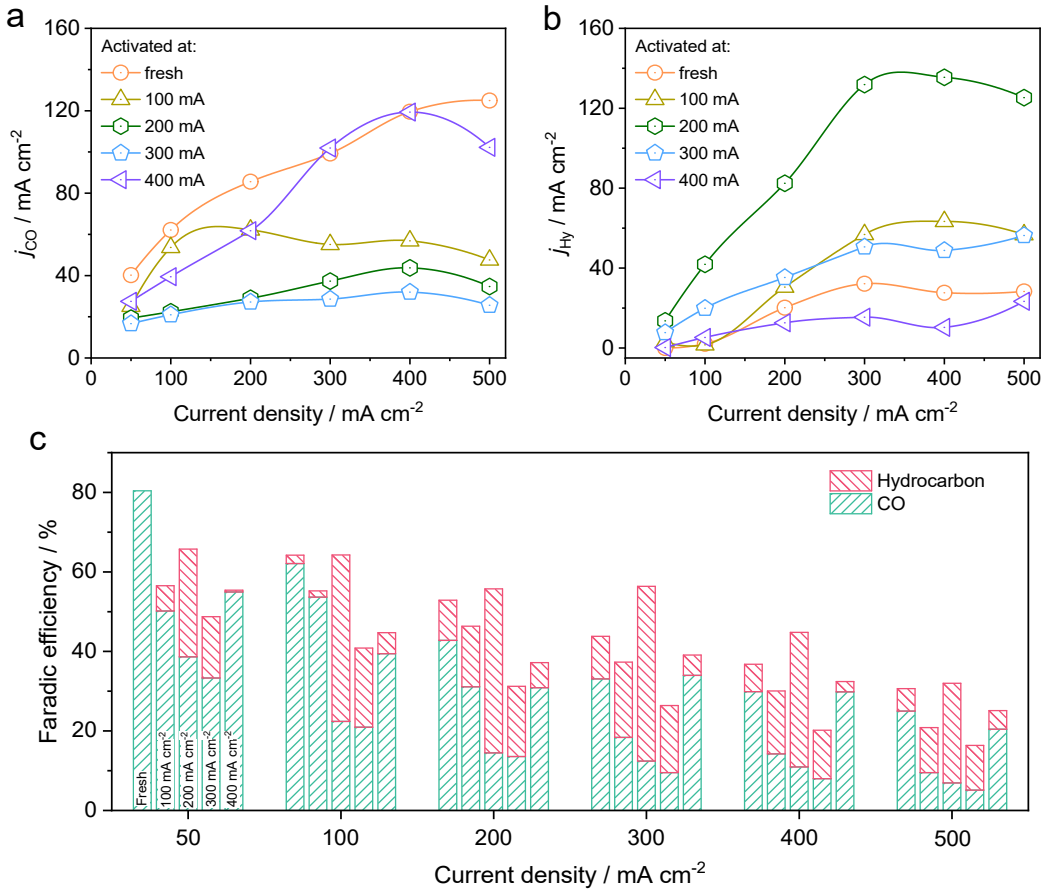

Figure S26. The partial current density of (a) CO and (b) hydrocarbon on Ag catalysts at various states. (c) The comparison of activation effect on CO and hydrocarbon selectivity.

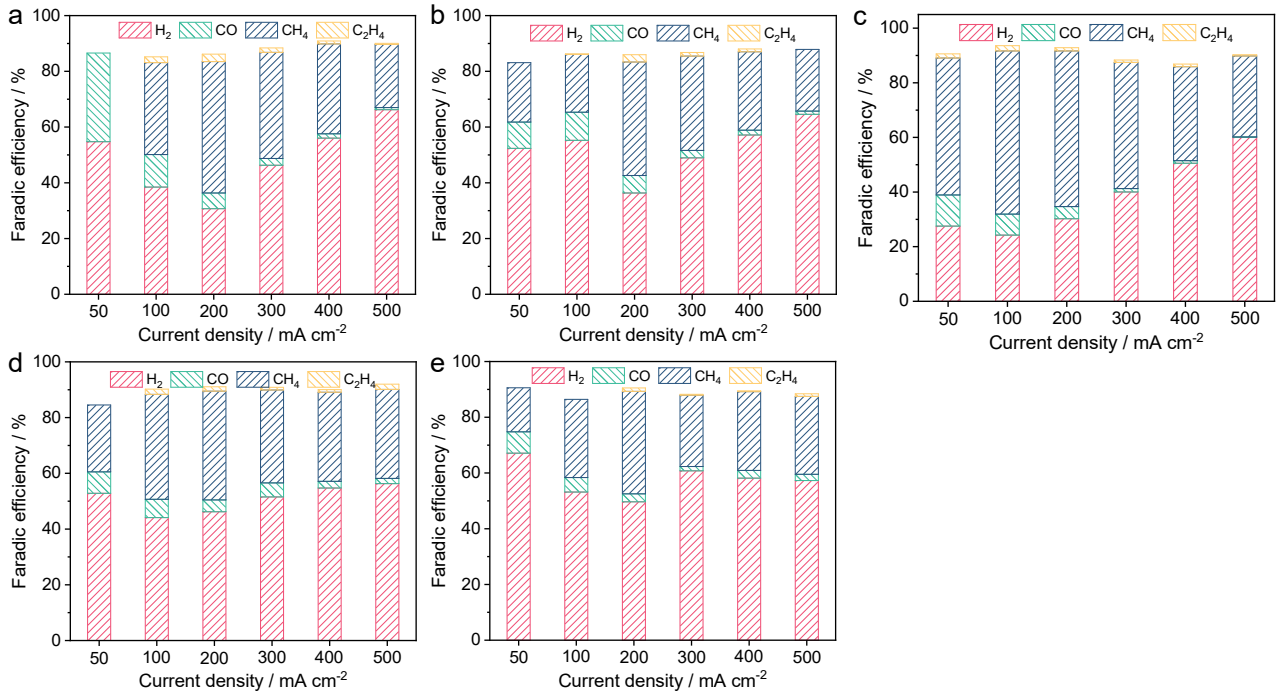

Figure S27. The CO_2RR performance of Ga catalysts (a) at fresh state, activated at (b) 100 mA cm^{-2}, (c) 200 mA cm^{-2}, (d) 300 mA cm^{-2} and (e) 400 mA cm^{-2}.

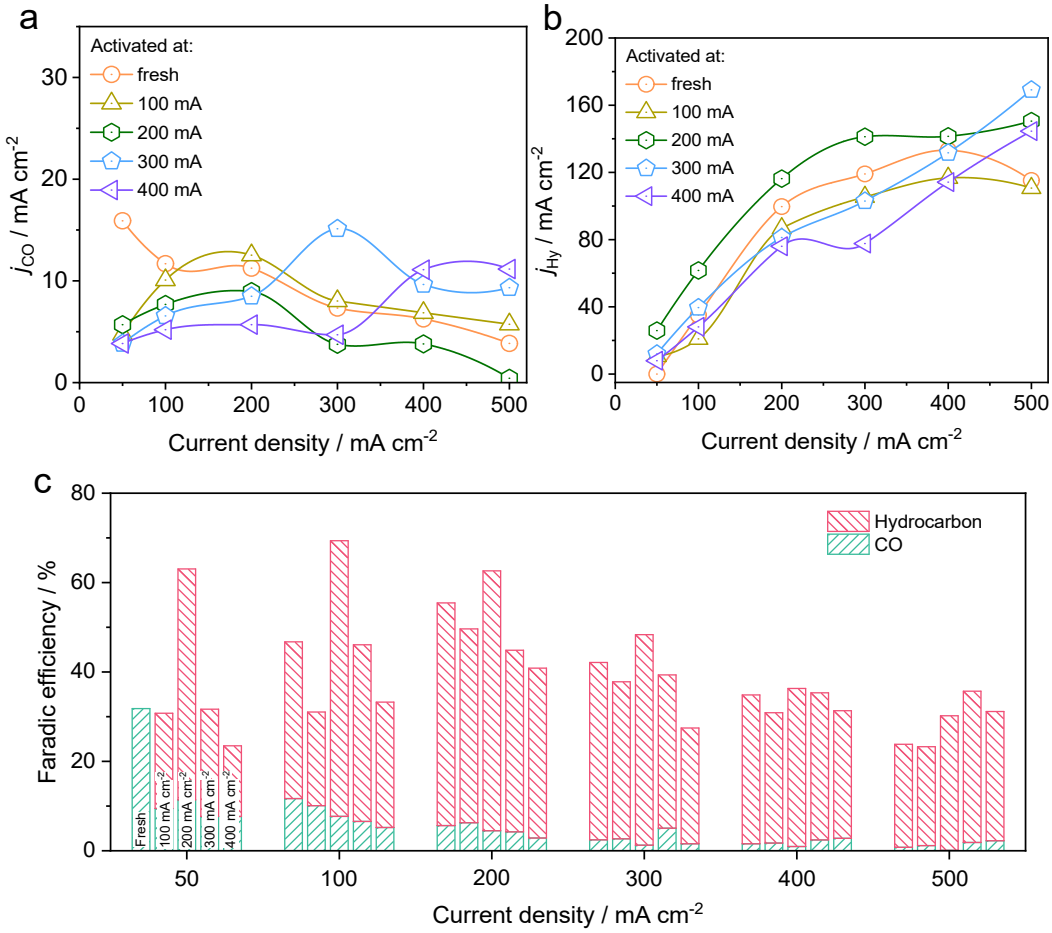

Figure S28. The partial current density of (a) CO and (b) hydrocarbon on Ga catalysts at various states. (c) The comparison of activation effect on CO and hydrocarbon selectivity.

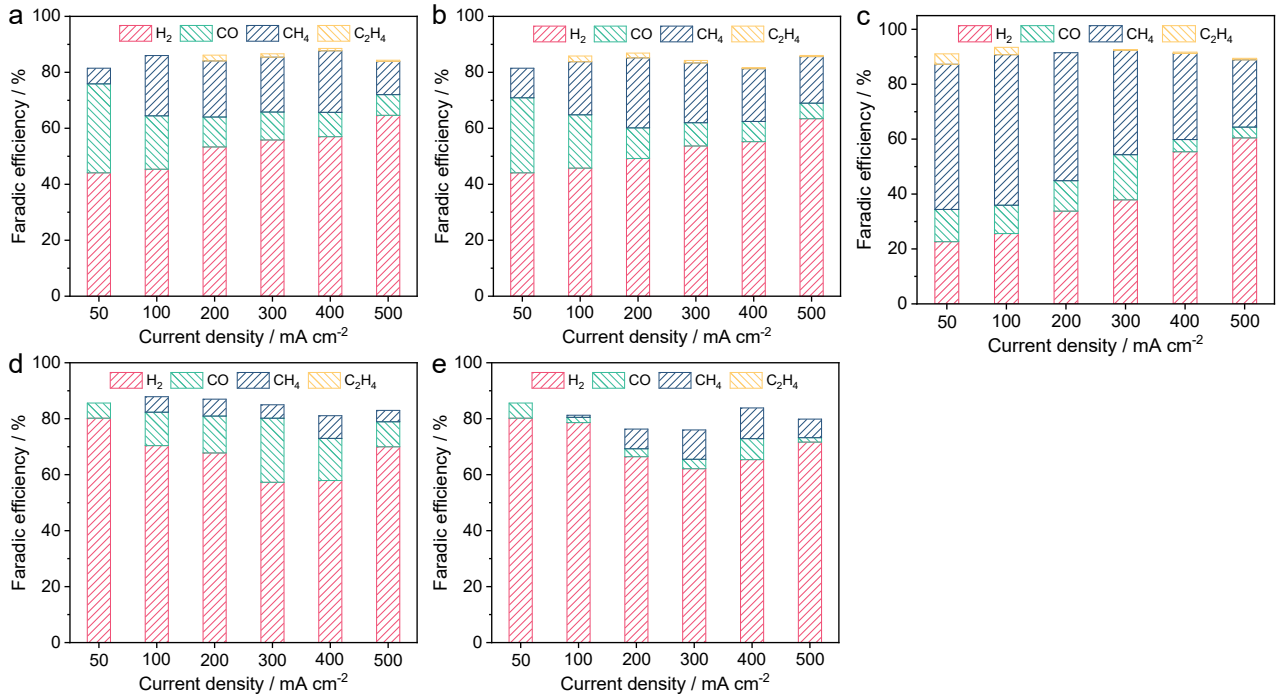

Figure S29. The CO_2RR performance of Zn catalysts (a) at fresh state, activated at (b) 100 mA cm^{-2}, (c) 200 mA cm^{-2}, (d) 300 mA cm^{-2} and (e) 400 mA cm^{-2}.

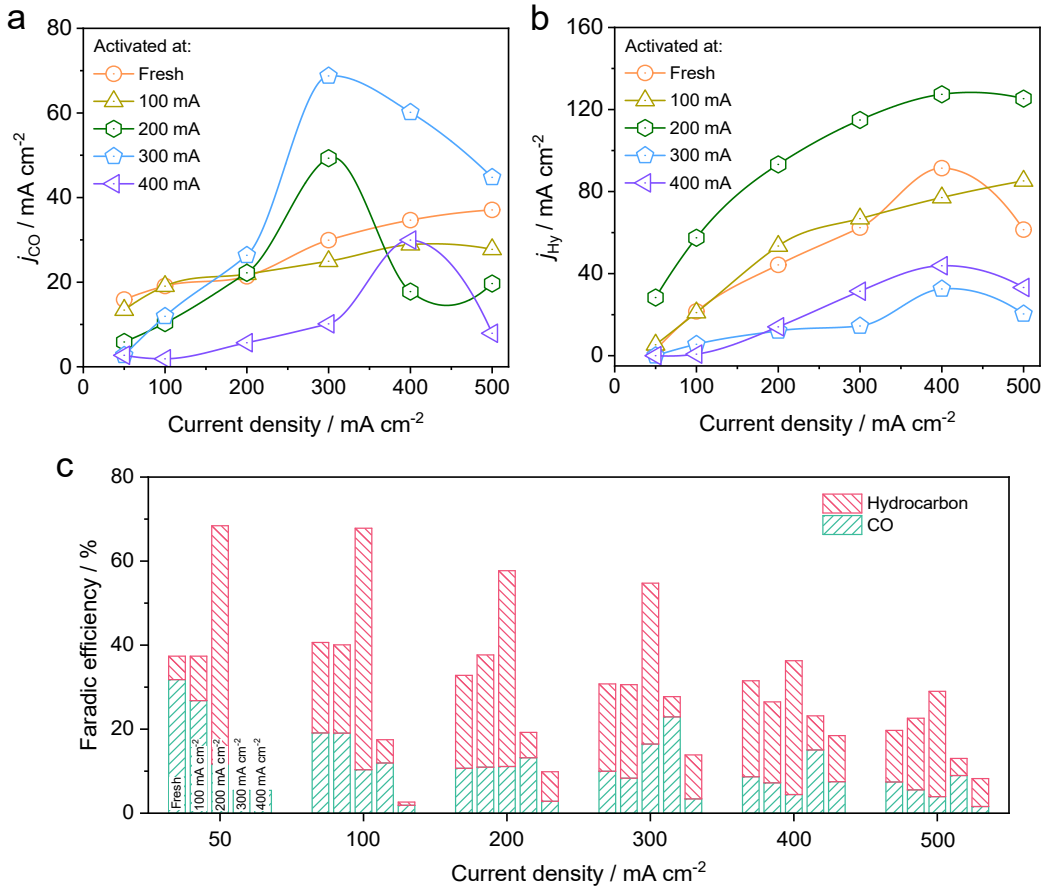

Figure S30. The partial current density of (a) CO and (b) hydrocarbon on Zn catalysts at various states. (c) The comparison of activation effect on CO and hydrocarbon selectivity.

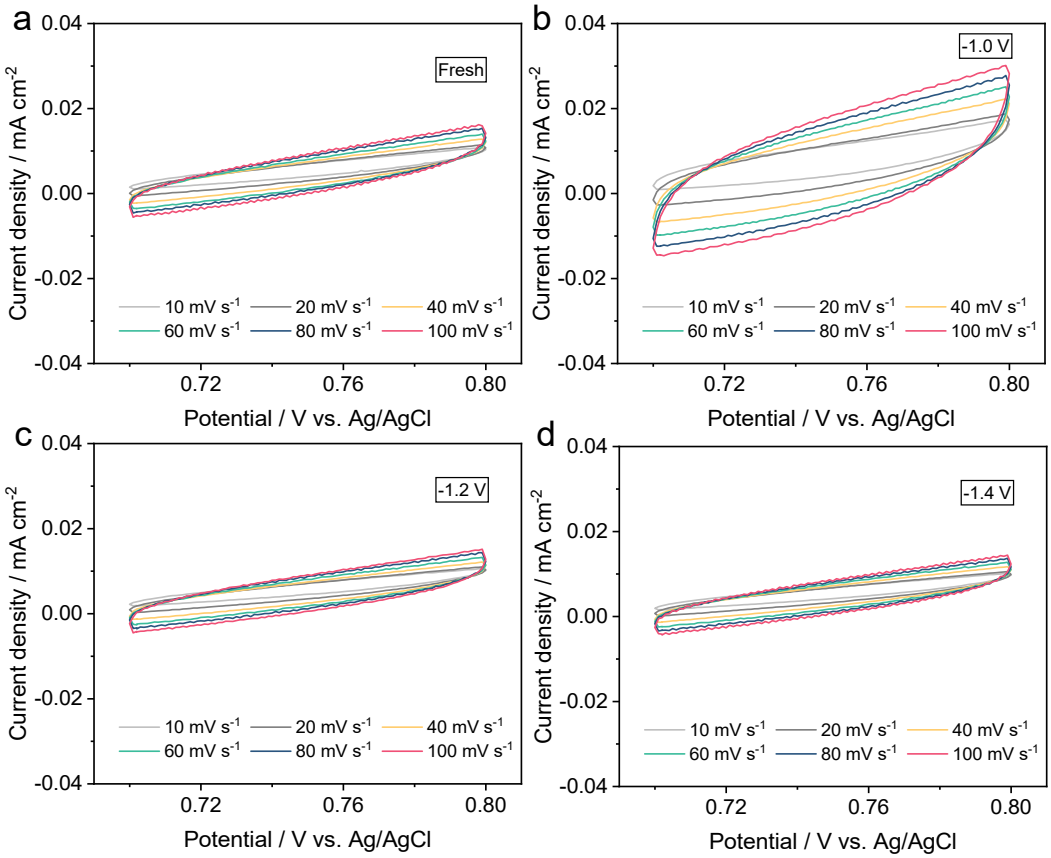

Figure S31. CV curves of Ag catalysts (a) at fresh state, activated at (b) –1.0 V, (c) –1.2 V, and (d) –1.4 V with different scan rates of 10-100 mV s^{-1}.

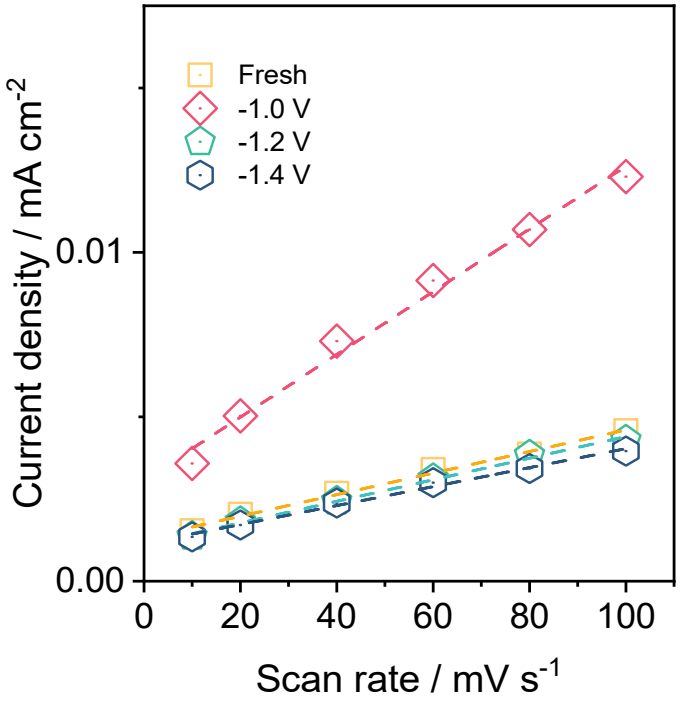

Figure S32. C_{dl} of Ag catalysts at various states.

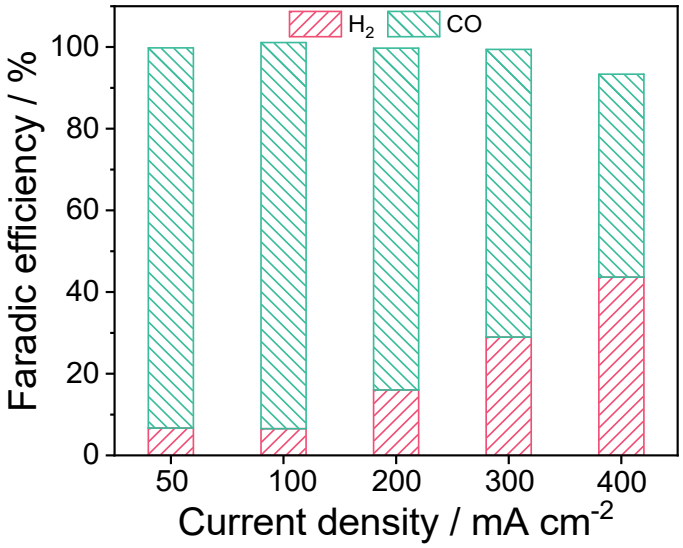

Figure S33. The CO_2RR performance of Au activated at 200 mA cm^{-2}.

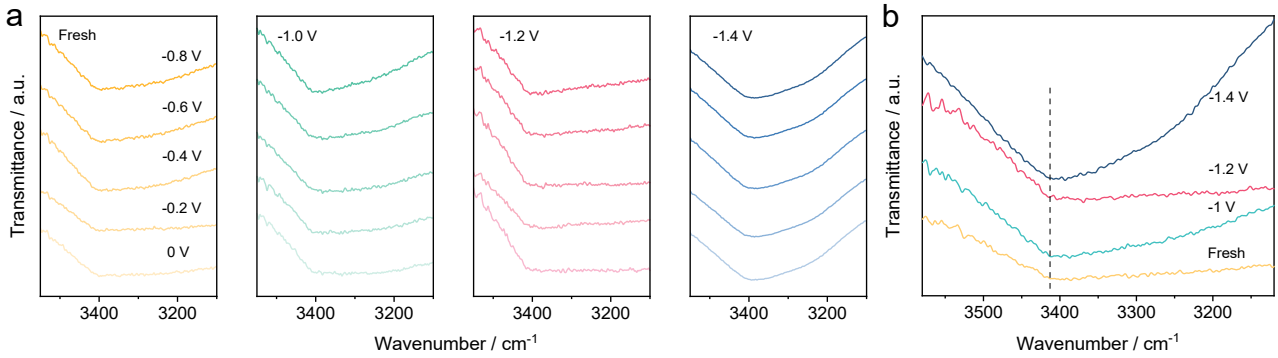

Figure S34. (a) The *in-situ* ATR-IR spectra of Au catalysts at various states, and (b) comparison of curves collected at –0.8 V vs. RHE.

Table S1. Reported CO_2RR performance on Pd catalysts.

Catalysts	Current density/mA cm^{-2}	Product	Faradic efficiency/%	Ref
Pd	202	CO	96.7	[6]
Pd nanocubes	4.2	CO	78	[7]
Pd film	1	CO	30	[8]
Pd	200	CH_4, C_2H_4	50	Our work

Table S2. The structures of *CO, *CHO and *COH under different numbers (n) of *OH adsorption.

n	*CO	*CHO	*COH
0 *OH	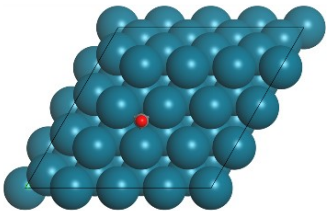	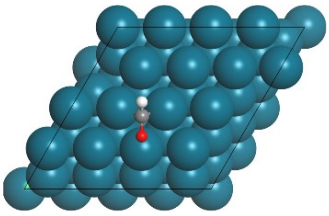	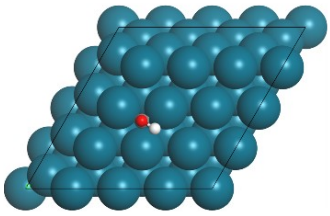
1 *OH	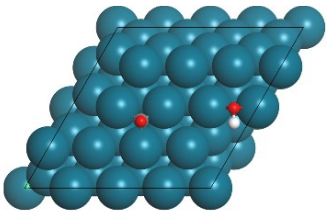	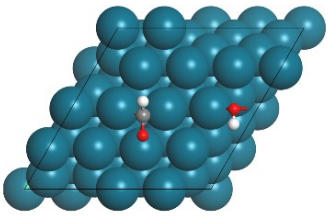	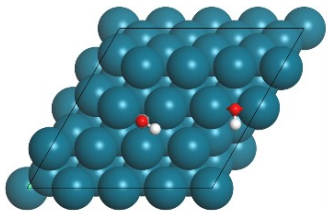
2 *OH	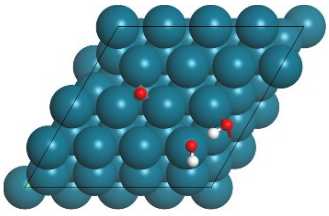	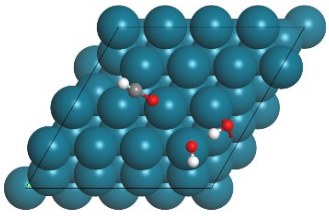	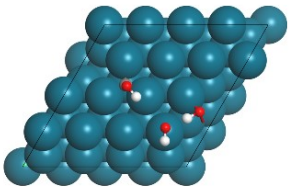
3 *OH	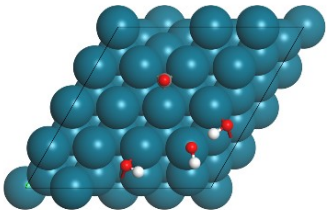	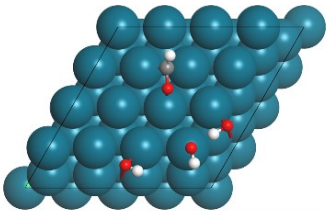	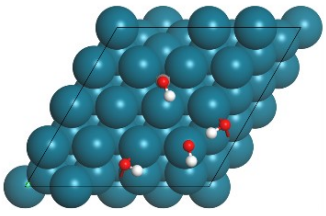
4 *OH	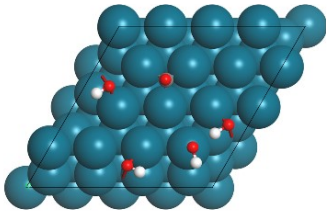	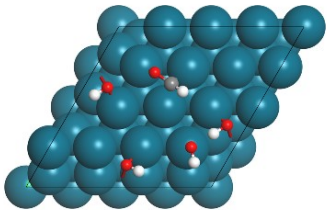	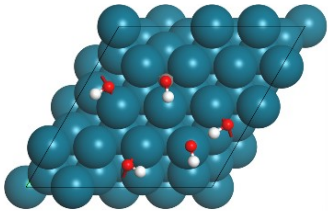
5 *OH	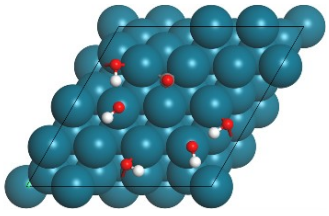	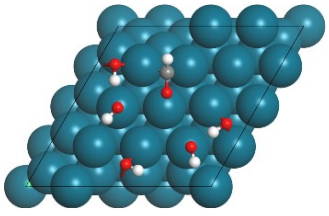	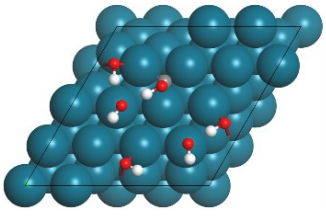
6 *OH	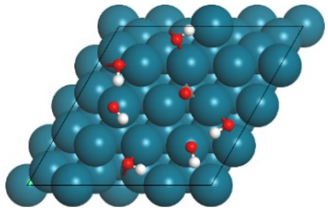	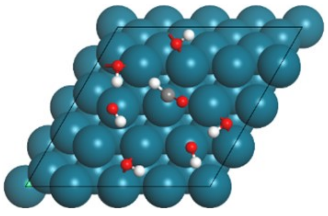	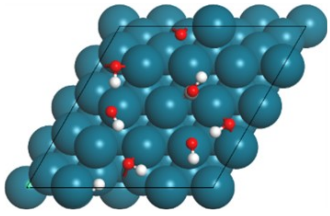

Table S3. The zero-point energies (ZPE) and entropies (–TS) of gas-phase species, *CO, *CHO and *COH under different numbers of *OH adsorption.

Species		ZPE (eV)	–TS (eV)
CO(g)		0.13	–0.61
H_2(g)		0.28	–0.40
0 *OH	*CO	0.19	–0.11
	*CHO	0.46	–0.12
	*COH	0.48	–0.12
1 *OH	*CO	0.19	–0.11
	*CHO	0.46	–0.12
	*COH	0.48	–0.13
2 *OH	*CO	0.19	–0.11
	*CHO	0.46	–0.12
	*COH	0.49	–0.11
3 *OH	*CO	0.19	–0.11
	*CHO	0.46	–0.11
	*COH	0.48	–0.12
4 *OH	*CO	0.19	–0.11
	*CHO	0.46	–0.12
	*COH	0.49	–0.12
5 *OH	*CO	0.20	–0.11
	*CHO	0.48	–0.11
	*COH	0.48	–0.10
6 *OH	*CO	0.20	–0.11
	*CHO	0.46	–0.11
	*COH	0.49	–0.11

Supplementary References

[1] a) G. Kresse, J. Hafner, *Phys. Rev. B* **1993**, *47*, 558-561; b) G. Kresse, J. Furthmuller, *Phys. Rev. B* **1996**, *54*, 11169-11186.

[2] J. P. Perdew, K. Burke, M. Ernzerhof, *Phys. Rev. Lett.* **1996**, *77*, 3865-3868.

[3] P. E. Blochl, *Phys. Rev. B* **1994**, *50*, 17953-17979.

[4] S. Grimme, J. Antony, S. Ehrlich, H. Krieg, *J. Chem. Phys.* **2010**, *132*, 154104.

[5] J. K. Nørskov, T. Bligaard, A. Logadottir, J. R. Kitchin, J. G. Chen, S. Pandelov, U. Stimming, *J. Electrochem. Soc.* **2005**, *152*, J23.

[6] J. Lee, J. Lim, C. W. Roh, H. S. Whang, H. Lee, *J. CO_2 Util.* **2019**, *31*, 244-250.

[7] X. Yang, J. H. Lee, S. Kattel, B. Xu, J. G. Chen, *Nano. Lett.* **2022**, *22*, 4576-4582.

[8] C. Hahn, D. N. Abram, H. A. Hansen, T. Hatsukade, A. Jackson, N. C. Johnson, T. R. Hellstern, K. P. Kuhl, E. R. Cave, J. T. Feaster, T. F. Jaramillo, *J. Mater. Chem. A* **2015**, *3*, 20185-20194.